Hofstetter, A., Bock, G. (2004): Shear-wave velocity structure of the Sinai subplate from receiver function analysis. - Geophysical Journal International, 158, 1, pp. 67—84.

DOI: http://doi.org/10.1111/j.1365-246X.2004.02218.x

Geophys. J. Int. (2004) **158,** 67–84 doi: 10.1111/j.1365-246X.2004.02218.x

Shear-wave velocity structure of the Sinai subplate from receiver function analysis

A. Hofstetter[1] and G. Bock[2,*]

[1] *Geophysical Institute of Israel, Lod, Israel. E-mail: rami@gii.co.il*
[2] *GeoForschungsZentrum, Potsdam, Germany*

Accepted 2003 November 9. Received 2003 November 9; in original form 2002 April 19

SUMMARY

Teleseismic data observed at seven broad-band stations located in and adjacent to the Sinai subplate were analysed using the receiver function method for estimating the velocity structure of the crust and upper mantle. The receiver function method is based on the analysis and interpretation of *P–S* converted phases and associated surface multiples that originate at seismic discontinuities beneath the receiver. The main converted *P–S* phases are from the base of a near-surface sedimentary layer located in the upper crust, at the Moho, in the subMoho upper mantle, at the 410- and 660-km seismic discontinuities. The velocity structure of the crust and the upper mantle varies within the Sinai subplate. A complicated crustal structure is suggested for the Cyprus arc, which marks the northern boundary of the Sinai subplate, with a Moho depth of 28 km. In the area of the Dead Sea Fault (DSF), which marks the eastern boundary of the Sinai subplate, Moho depth increases from north to south from approximately 27 km beneath station MRNI located in northern Israel to approximately 34 km beneath station EIL located north of the Gulf of Aqaba. Away from the DSF, a crustal thickness of 34–36 km is indicated at HITJ located in the Arabian Plate and KEG located in the African Plate. A low-velocity zone (LVZ) beginning at approximately 60-km depth is inferred beneath stations located close to the DSF. This boundary is interpreted as the lithosphere–asthenosphere boundary (LAB). The shallow LAB may be the top of a highly deformed mantle zone and may have facilitated the formation of the DSF some 15 Ma.

Key words: crustal structure, Cyprus arc, Dead Sea Fault, mantle discontinuities, Moho discontinuity, receiver functions.

1 INTRODUCTION

Receiver function analysis is a powerful tool for obtaining information about crust and mantle structure beneath a seismic station. The method makes use of waves that are converted from *P* to *S* at seismic discontinuities beneath the station. The theoretical background of the technique has been developed and described in detail (e.g. Burdick & Langston 1977; Langston 1977; Owens *et al.* 1984; Ammon *et al.* 1990). In comparison with controlled source seismic experiments, the receiver function method has a limited resolution within the crust because of the lower signal frequencies used, but depth penetration is virtually unlimited because earthquakes are used as sources, providing a better resolution than any other existing method. Thus the receiver function method complements methods of controlled source seismic experiments, which employ shorter period waves and thus achieve a higher resolution at shallow depths.

Until recently, the coverage of broad-band stations in the Middle East and the eastern Mediterranean was rather sparse. Newly installed stations, for example CSS, HITJ and MRNI (Fig. 1), provide a wealth of new data in addition to observations from stations BGIO and KEG, in contrast to the small number of observations that were presented for the latter in the study of Sandvol *et al.* (1998b). These new data will improve our knowledge of the structure of the crust and the upper mantle of the Sinai subplate. The goal of this study is to use the receiver function method, taking advantage of these new recordings, to determine the velocity structure beneath broad-band stations in Cyprus, Egypt, Israel and Jordan. Besides crustal structure and thickness, we also investigate seismic boundaries in the upper mantle and in the transition zone between the upper and lower mantle, bounded by the 410- and 660-km seismic discontinuities.

2 TECTONIC SETTING

The Sinai subplate forms an elongated triangle bordered by the Cyprus arc in the north, the Dead Sea Fault (DSF) and Gulf of Aqaba along to the east, and the Gulf of Suez with unclear continuation into the Mediterranean to the west (following Salamon *et al.* 1996 see Fig. 1). The southernmost part of the subplate is the Sinai Peninsula. Seismic refraction studies of the crust of Israel and Jordan (Ginzburg

*Deceased (2002 November 6).

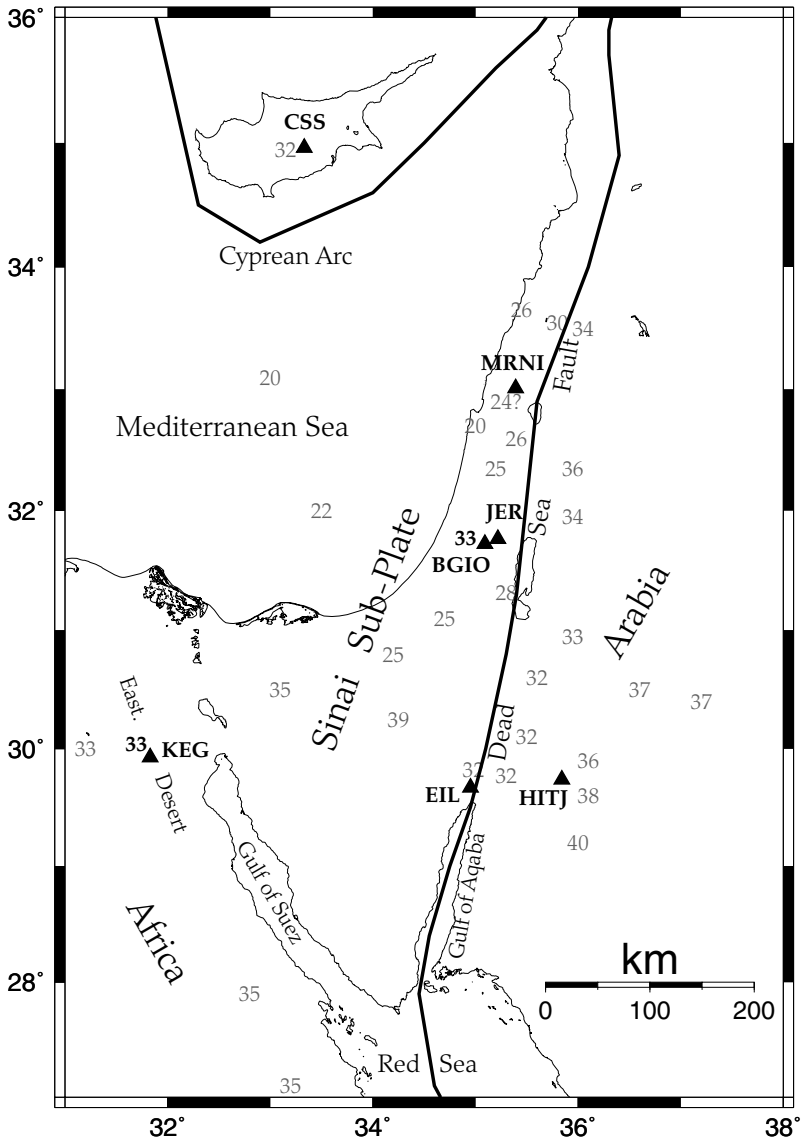

Figure 1. Schematic plot of the main tectonic features and faults (thick solid line) surrounding the Sinai subplate and the broad-band stations (solid triangle) that were used in this study. The grey numbers represent the crustal thickness at selected locations, as obtained in refraction studies; the bold black numbers are the crustal depths reported by Sandvol *et al.* (1998b).

et al. 1979a,b; Makris *et al.* 1983; El-Isa *et al.* 1987a,b; El 1990) support the view that the Sinai subplate is a transition zone between the thick continental crust of the Arabian Shield, namely the Sinai peninsula and Jordan, and the relatively thin oceanic or intermediate crust under a relatively thick Mesozoic–Cenozoic sedimentary layer of the eastern Mediterranean Sea (Makris *et al.* 1994).

Grey and black numbers in Fig. 1 show the crustal thickness at selected locations in the Sinai subplate and adjacent regions, obtained from refraction studies (Ginzburg *et al.* 1979a,b, 1981; Makris *et al.* 1983; El-Isa *et al.* 1987a,b; Meshref 1990), gravimetric studies (Kamal *et al.* 1993; Al-Zoubi & Ben-Avraham 2002; Ben-Avraham *et al.* 2002) and a receiver function study (Sandvol *et al.* 1998b). The regional trend of the crustal structure is the gradual thinning of the crust towards the north and northwest. The geological and tectonic settings do not suggest a complicated velocity structure in the vicinity of any of the stations. Southeast of station HITJ (Fig. 1), towards the Arabian Peninsula, the crust thickens to approximately 36–40 km in the Arabian Shield and the Arabian Platform based on regional waveform modelling (Rodgers *et al.* 1999), refraction seismic studies (El-Isa *et al.* 1987a,b), a gravimetric study (Al-Zoubi & Ben-Avraham 2002) and receiver function analysis (Sandvol *et al.* 1998a; Kumar *et al.* 2002). The crust is approximately 36 to 39-km thick WNW of EIL and thins towards the centre of the Sinai subplate to approximately 24 km inland near MRNI and 20 to 22 km in the Mediterranean Sea (Ginzburg *et al.* 1979a,b; Ginzburg & Folkman 1980; Makris *et al.* 1983; Ginzburg *et al.* 1994, see Fig. 1). The crust west of KEG is continental in nature with a thickness of 33 km (Meshref 1990).

The break-up of the Arabian massif created the Red Sea, Gulf of Suez and Gulf of Aqaba, part of the DSF (see Fig. 1). In a recent detailed study Sneh (1996, and references therein) showed that from 30 to 16 million BP mainly horizontal motion occurred along the DSF. Vertical uplift on both sides of the DSF, accompanied by significant volcanic activity started approximately 4–5 Ma (i.e.

Picard 1951; Garfunkel & Horowitz 1966; Garfunkel 1981; Heimann *et al.* 1996; Matmon *et al.* 2000).

The oceanic opening of the Red Sea started less than 20 Ma (Courtillot *et al.* 1999) and gave rise to two cycles of magmatic activity that migrated northward of the Afar covering large areas of the Arabian massif (i.e. Baker *et al.* 1996; Hofmann *et al.* 1997; Segev 2000). As part of the tectonomagmatic activity of the mantle plume in the Afar, Red Sea and southwestern part of Arabia, during the Oligocene to present, the Arabian massif was subjected to a stage of uplift and break-up (Camp & Roobol 1992; Courtillot *et al.* 1999). These authors described the contemporaneous magmatism in the west of the Arabian Peninsula as the upwelling of hot asthenosphere that is still active at present. North of the Gulf of Aqaba, volcanic rocks are observed on both sides of the DSF, with no magmatic activity within the fault zone and average heat flow values in the Dead Sea basin (Ben Avraham *et al.* 1978).

A series of seismological studies describe the complex velocity structure of the crust and upper part of the upper mantle beneath the eastern Mediterranean Sea, Arabian Shield, Arabian Platform and Turkish–Iranian plateau. These studies are based on traveltime residuals from regional earthquakes (Hearn & Ni 1994), regional waveform modelling and surface wave group velocities (Rodgers *et al.* 1999), and regional wave propagation (Rodgers *et al.* 1997; Mellors *et al.* 1999; Gök *et al.* 2000; Sandvol *et al.* 2001). The main results of these studies are:

(1) Low *Pn* velocity ($<$7.9 km s^{-1}) and blocked *Sn* propagation is observed in the Turkish–Iranian Plateau.

(2) *Pn* velocities beneath the eastern Mediterranean Sea are approximately 8.0 km s^{-1} or slightly higher.

(3) Inefficient *Sn* propagation and low *Pn* velocities are observed along most of the DSF.

(4) Waveforms from earthquakes in the Gulf of Aqaba, observed at stations in the Arabian Peninsula, exhibit weak body phases and *P*- and *S*-wave velocities immediately below the Moho are slightly lower in western Arabia and slightly higher for the Arabian Platform.

(5) The region of inefficient *Pn* and *Sn* propagation coincides with a region of recent volcanism in western Arabia.

Furthermore, for western Arabia Knox *et al.* (1998) found seismic velocities that are 0.2 to 0.8 km s^{-1} lower than the PREM model at a depth of 100 km. In addition, Debayle *et al.* (2001), based on observations of Rayleigh waves, suggested a deeply rooted low-velocity anomaly in the upper mantle.

3 DATA

Fig. 1 shows the broad-band stations that were used in this study. The station coordinates, operating periods and the number of events used in this study are listed in Table 1. Station KEG in Egypt is jointly operated by the National Research Institute of Astronomy and Geophysics, Egypt, and MedNet, Istituto Nazionale di Geofisica e Vulcanologia, Italy; it started recording in 1990 December. During 1994 May a broad-band station BGIO was deployed at Bar Giora, near Jerusalem (Shamir 1995; Hofstetter 1996), and later in 1996 May it was transferred to Jerusalem, JER (former WWSSN site; Fig. 1). The Geophysical Institute of Israel (GII) operates stations EIL (former WWSSN) and MRNI in Israel in cooperation with the GEOFON programme of GeoForschungsZentrum (GFZ), Germany. The broad-band station CSS in Cyprus is jointly operated by the Geological Survey, Cyprus, GFZ and GII. The broad-band station HITJ in Jordan is jointly operated by the Natural Resources Authority, Jordan, and Lawrence Livermore National Laboratory, USA.

Table 1. Broad-band stations and numbers of events used in this study.

Station	Latitude (north)	Longitude (east)	Altitude (km)	Operating period	Number of events
KEG	29.928	31.829	0.460	1990/12–1999/12	44
BGIO	31.722	35.092	0.760	1994/5–1996/4	79
JER	31.772	35.197	0.770	1996/5–present	54
EIL	29.670	34.951	0.200	1997/1–present	52
MRNI	33.009	35.391	0.896	1998/9–present	66
HITJ	29.739	35.842	1.263	1998/9–present	31
CSS	34.962	33.331	0.396	1998/12–present	59

We selected 284 events for the period from 1994 to 2000 covering an epicentral range of 35° to 90° and a magnitude range $5.6 \leq m_b \leq 7.8$, based on the National Earthquake Information Service catalogue. The distribution of the selected events is shown in Fig. 2. Most of the events studied lie in the northeast and southeast quadrants. The azimuthal distribution of events is particularly good for stations KEG, EIL and JER.

4 RECEIVER FUNCTION PROCESSING

A detailed description of the processing method that we adopted is given by Kind *et al.* (1995) and Yuan *et al.* (1997). Here we briefly describe the steps taken. All the processing was carried out within the framework of the SEISMICHANDLER analysis tool package developed by Stammler (1993). Each seismogram of the *P*-wave group is rotated from the original Z, NS and EW components into the ray coordinate system L, Q and T. The L, Q and T components contain mainly *P*, *SV* and *SH* energy, respectively. The *P–SV* converted waves are determined by the *S*-velocity structure beneath the station. The existence of anisotropy or lateral heterogeneity is reflected by energy in the T component. The receiver function method uses a process of deconvolution to remove the source-time function from the three components (L, Q and T). This is performed by deconvolving the *P* waveform on the L component from the Q and T components (see Langston 1979; Owens *et al.* 1984). All components are then normalized to the maximum of the L component. The resultant time function on the Q component approximates the *SV* response of the structure beneath the receiver to a plane *P*-wave incident from below. We refer to the deconvolved Q component or *SV* seismograms as the receiver function of the station. The deconvolved L-component seismograms are referred to as the *P*-wave seismograms.

To improve the signal-to-noise ratio, we sum the rotated and deconvolved receiver functions from earthquakes over a wide range of distances (35° to 90°) and backazimuthal coverage (ideally up to 360°). As the delay times of converted phases depend on the slowness of the incident *P* wave and the discontinuity depth, we apply a move-out correction for *P–S* converted phases relative to a reference slowness of 6.4 s deg^{-1} (70°). The move-out correction is dynamically applied to the *SV* seismograms. After move-out correction, all *P–S* converted phases should align parallel to the *P*-wave arrivals when plotted against distance, whereas multiples of type *Ppps* and *Ppss* and higher order will not. Move-out correction is particularly important for studying converted phases that originate deeper in the mantle, e.g. at the 410- and 660-km discontinuities.

5 RECEIVER FUNCTION RESULTS

Examples of move-out-corrected seismograms and the resulting stacks are shown in Figs 3 and 4. The seismograms were low-pass

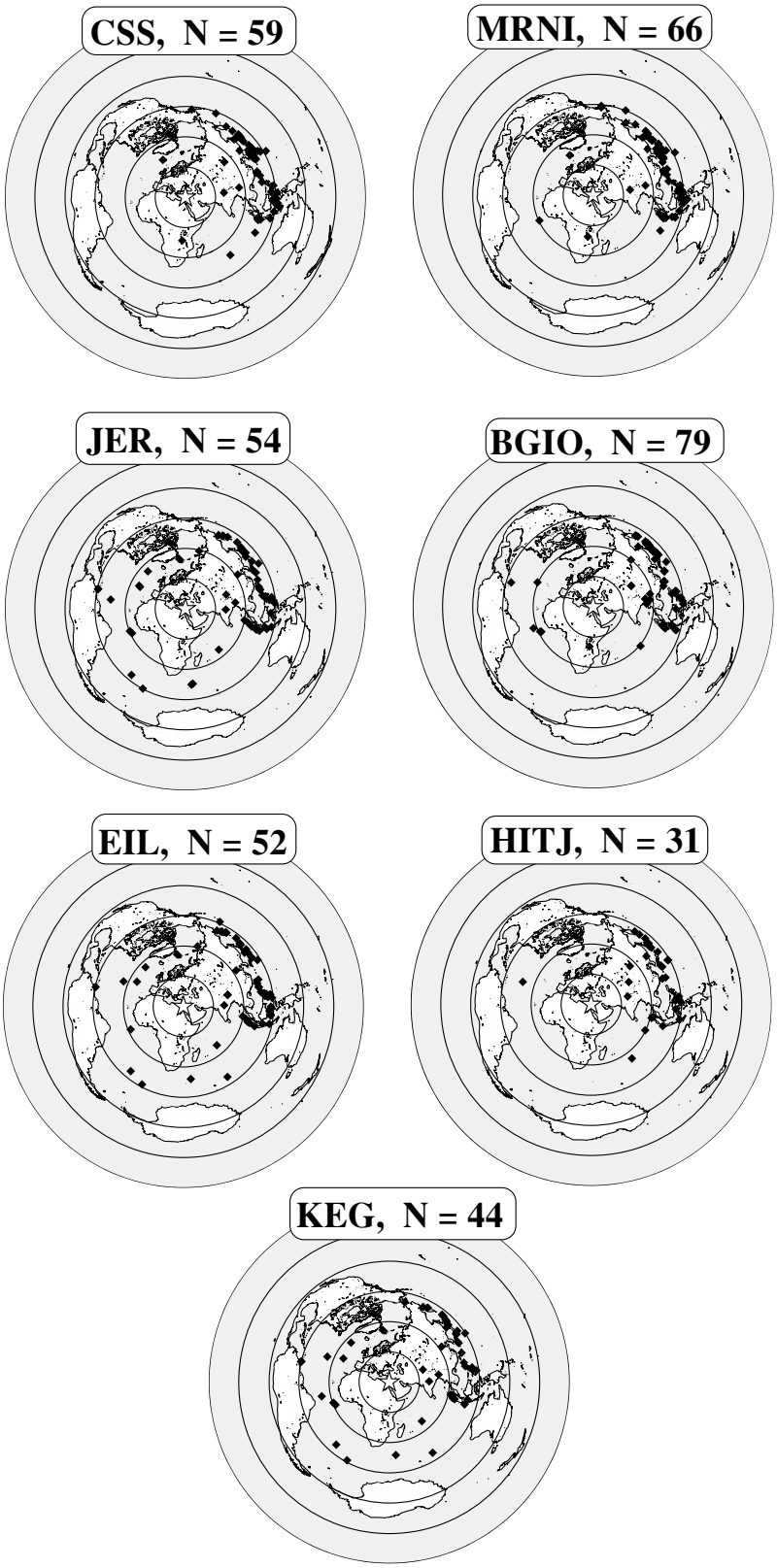

Figure 2. Distribution and number of earthquakes used in this study plotted in an azimuthal equidistant projection with the station location (star) in the centre. Concentric circles about the centre are plotted in 30° intervals.

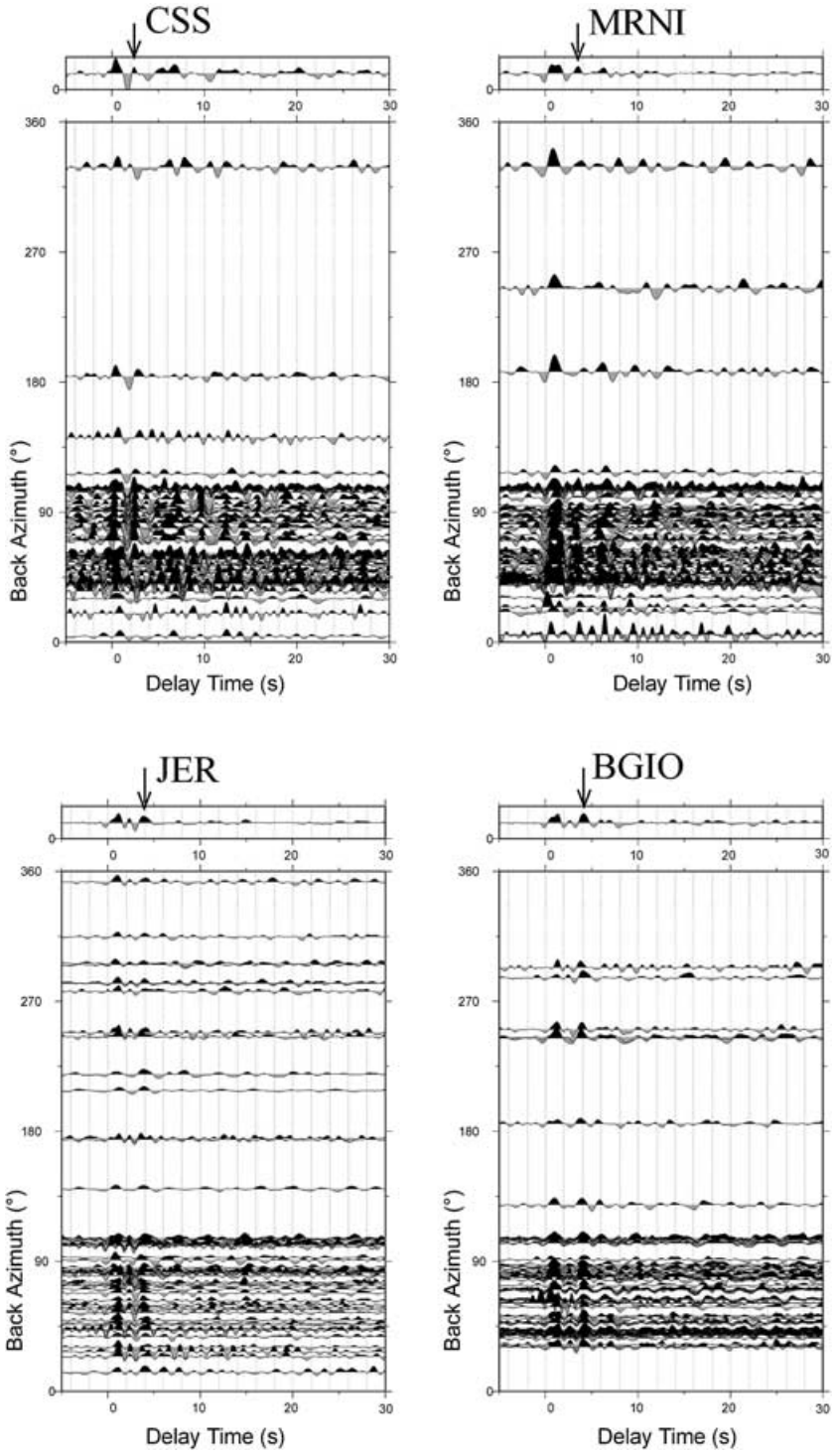

Figure 3. Receiver function seismograms plotted as a function of back azimuth. The zero-phase *P* wave defines the zero time. The traces are move-out-corrected relative to a reference slowness of 6.4 s deg^{-1} and then stacked (uppermost trace). Stacked traces are also shown in Fig. 4. Arrows indicate interpreted *P–S* conversions from crust–mantle boundary. Traces are low-pass filtered with cut-off at 0.5 Hz.

filtered with a cut-off frequency at 0.5 Hz. In Fig. 3, the receiver functions are sorted by backazimuth (azimuth from station to epicentre). The stacked seismograms are displayed on top of each station panel and also shown separately in Fig. 4. In both the single sections and the stacked seismograms, we can distinguish several phases that originate in the crust and upper mantle. The phase marked in Figs 3 and 4 by an arrow is interpreted as a *P–S* conversion from the crust–mantle boundary. The delay time of this phase varies considerably from station CSS in Cyprus to KEG in Egypt, suggesting that large variations in crustal thickness occur. All stations exhibit a strong phase at a delay time of less than 1 s. This phase represents a *P–S* conversion from a shallow interface in the uppermost 10 km of the crust. Multiples associated with this conversion can be recognized on all traces (Fig. 4). For example, the minimum seen between the

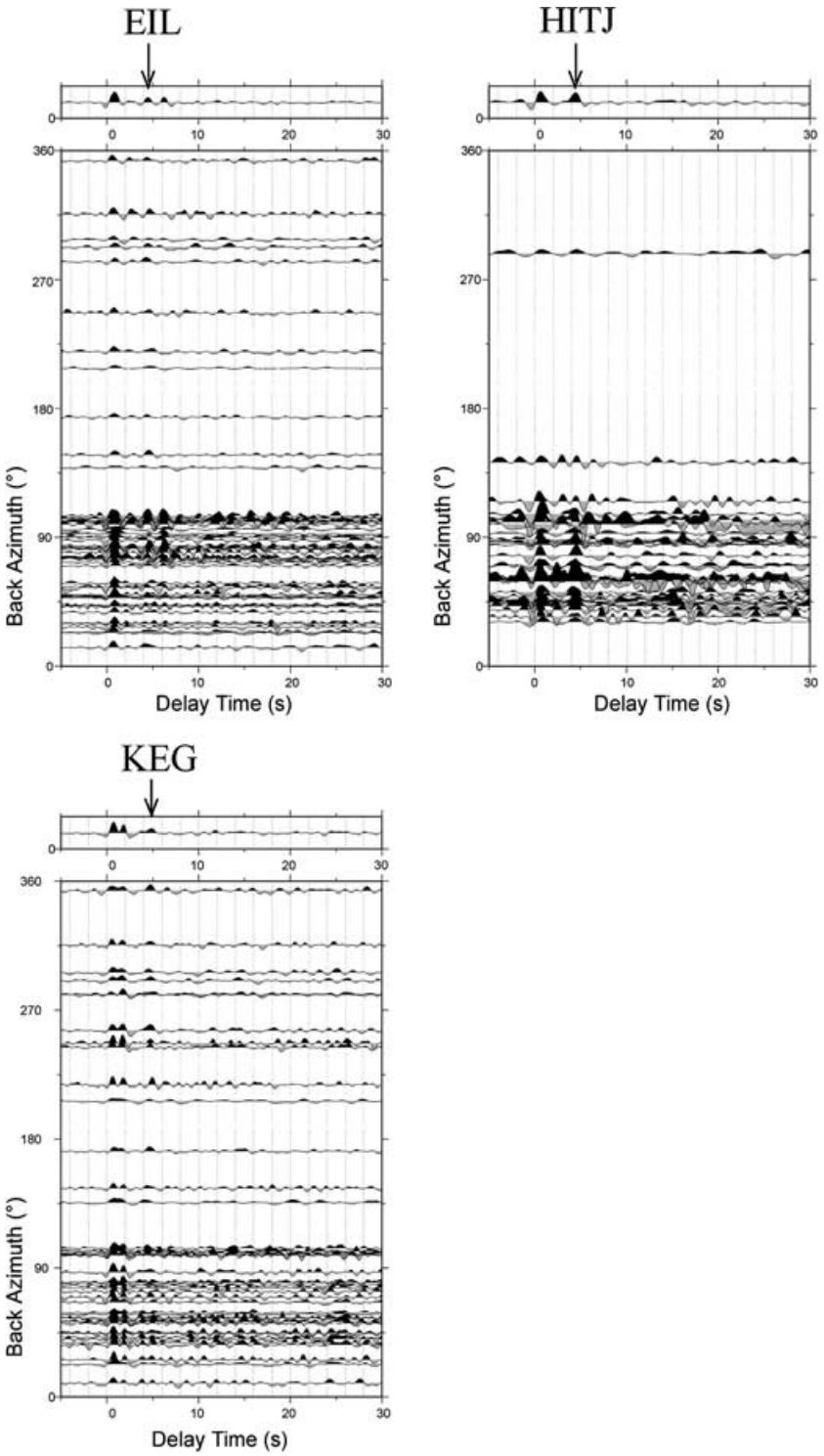

Figure 3. *(Continued)*

shallow conversion and the *P–S* conversion from the Moho is particularly prominent at CSS, MRNI and KEG. It represents a multiple of type *Ppss*, which is converted at the surface from an incident *P* wave to an *S* wave and then subsequently reflected at the top of the interface. Its polarity is opposite to that of the primary conversion. The multiple *Ppps* arrives closer to the primary conversion; separation of primary conversion and *Ppps* multiple is apparent at MRNI and most pronounced at KEG. The *Ppps* multiple has the same polarity as the primary *P–S* converted phases.

To investigate the *SV* wavefield in the long-period range, we applied a low-pass filter with cut-off frequency at 0.2 Hz and repeated the summation of *P–S* move-out corrected traces. The stacked seismograms are shown in Fig. 5. It is obvious, through comparison with Fig. 4, that the resolution of crustal phases has deteriorated.

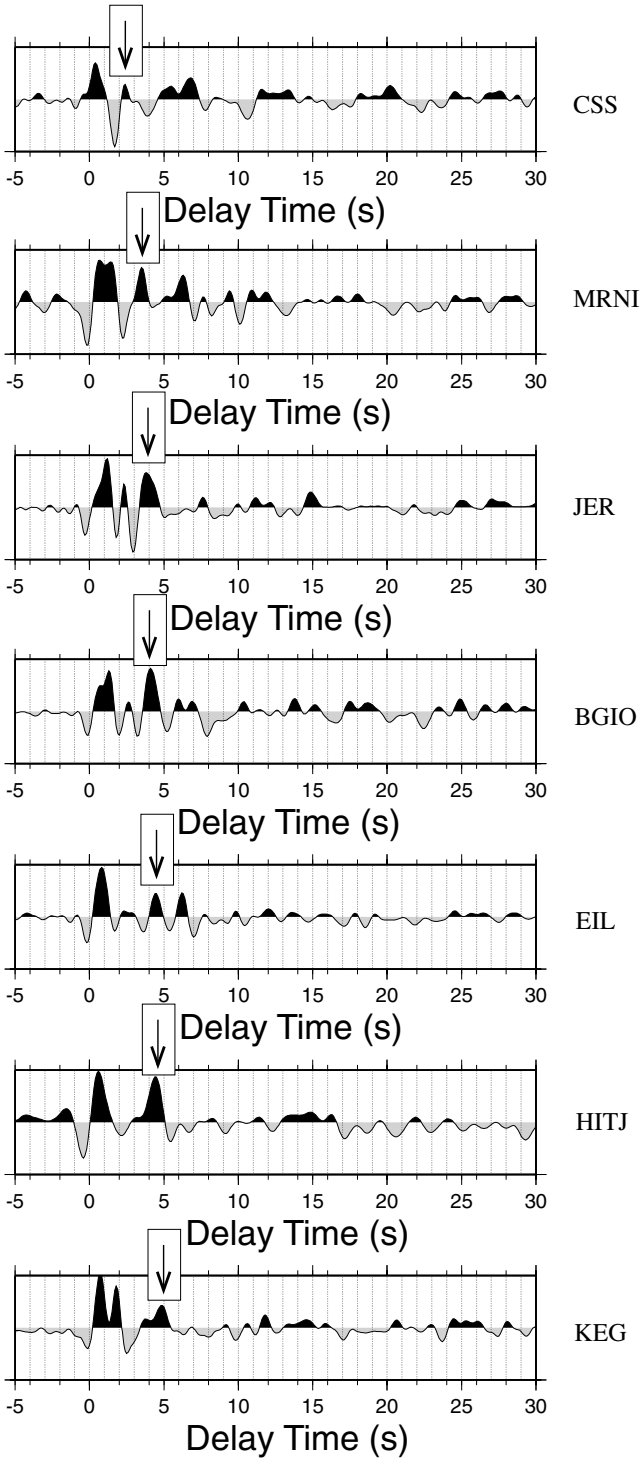

Figure 4. Stacked receiver functions for the stations investigated and shown in Fig. 3. Arrows point to P_MS, the P–S converted phases from the Moho.

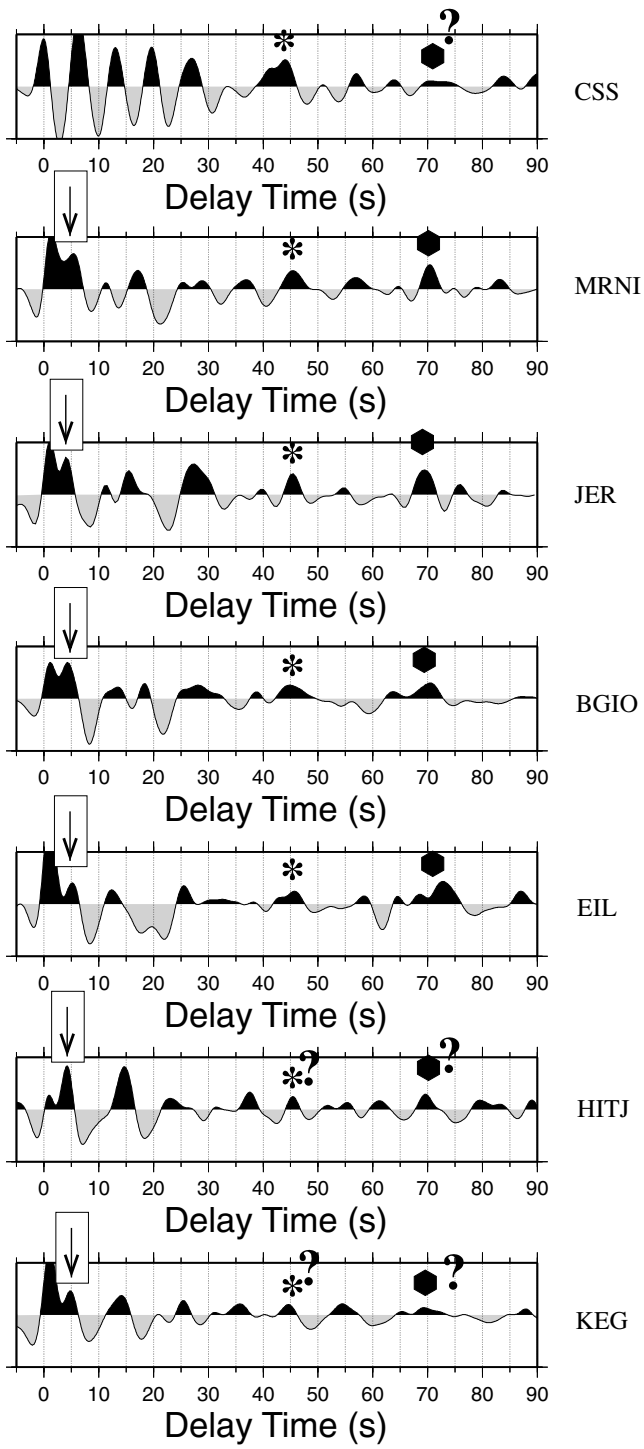

Figure 5. Stacked receiver functions, low-pass filtered with a cut-off frequency at 0.2 Hz. This emphasizes energy in the long-period band. The P_MS phase is not always so well resolved as in the seismograms of Fig. 4. Multiples associated with P_MS are seen between approximately 15 and 20 s delay time. The negative amplitude seen at 5–10 s probably represents a P–S conversion from an upper-mantle low-velocity zone (LVZ) at the stations EIL, BGIO, JER and MRNI, while at HITJ and KEG this may be related to multiples from crustal phases. Identification as upper-mantle phases is indicated by associated multiples arriving between 20 and 30 s at EIL, BGIO, JER and MRNI.

However, the low-pass filtered seismograms are a considerable aid in the identification of both mantle discontinuities and multiples associated with P–S conversion from the crust–mantle boundary and from an interface in the uppermost mantle where velocity decreases with depth. P–S converted phases from the 410- and 660-km discontinuities are marked by asterisks and filled hexagons, respectively. These were identified by slowness analysis of the converted

phases following the method developed by Vinnik (1977). Symbols accompanied by question marks indicate phases that do not stand out clearly against neighbouring phases, but whose traveltimes are consistent with *P–S* conversions from the 410- and 660-km discontinuities.

Multiples associated with *P–S* conversions from the Moho are more easily recognized on the long-period receiver function stacks of Fig. 5. While they can also be identified at other stations, the multiples are particularly clear at station HITJ where the positive phase at approximately 14 s delay time is the *Ppps* multiple followed by the *Ppss* multiple at approximately 18 s, which has a negative polarity.

6 RECEIVER FUNCTION MODELLING

Traditionally, receiver functions are inverted for an *S*-wave velocity model as a function of depth. There is no guarantee that a unique inversion result will be obtained: it is advantageous therefore to use *a priori* information available for the region under investigation. To overcome the problem of non-uniqueness, we employed two different methods of receiver function inversion. Both methods seek to minimize the differences between observed and synthetic receiver functions. Synthetic receiver functions are calculated with the Thomson–Haskell matrix method for a plane *P* wave incident from below on a layered elastic medium where seismic velocities vary only as a function of depth.

The method described by Kind *et al.* (1995) is a non-linear inversion scheme, which requires the definition of an initial velocity–depth function, and then iteratively improves the model by matching observed and synthetic receiver functions. The final result depends to some extent on the initial model and the parametrization of the model. Gradients are approximated by a sequence of relatively thin layers with a gradual trend of increase (or decrease) of velocity, but with constant velocity in each layer. For the definition of the initial model at a given broad-band station we use *a priori* knowledge of the structure of the crust and upper mantle based on reflection and refraction studies (Ginzburg *et al.* 1979a,b; Makris *et al.* 1983; El-Isa *et al.* 1987a,b; Ben-Avraham & Ginzburg 1990; El 1990; Hofstetter *et al.* 1991; Feigin & Shapira 1994; Hofstetter *et al.* 2000). Based on these studies we determined *S*-wave velocities assuming a *Vp*/*Vs* ratio of 1.73 for the crust and 1.80 for the upper mantle, where the latter are global averaged values (Christensen 1996). We use the time interval from 5 s prior to the zero-phase *P* wave to 30 s after for fitting the synthetic and observed waveforms. These include all crustal and upper-mantle conversions and the strongest multiples.

Fig. 6 presents the results of the receiver function inversion for the individual stations. The initial velocity–depth functions (lower signal on the right side) and the final model obtained after several iterations (middle trace on the right side) are shown. In the seismogram parts of the figure, the deconvolved *P*-wave seismogram is shown on top. Dashed lines depict the observed receiver functions and these are overlain on the synthetics for the initial model and for the final model. We followed a strategy of keeping the velocity models as simple as possible while still taking into account the results of previous crustal studies and, therefore, used a rather simple model that avoids small-scale unrealistic anomalies. Thus, the model explains the main features of the crust and upper mantle that are coherent across most of the records, specifically, the sedimentary sequence, upper and lower sections of the crust, Moho discontinuity and any large-scale structure in the upper mantle. The results shown in Fig. 6 represent the end product after much trial and error modelling. The synthetic seismogram (Q component) that was derived from the initial model at a given station is taken as the first approximation. To improve the fit between the synthetic and observed waveforms, we slowly change the parameters of the model each time, essentially applying a grid search method. Thus we were searching for the best fit, over a large velocity space, thickness and *Vp*/*Vs* ratio for all layers, until we reached a satisfactory fit. In addition, we used a large number of starting models, thus testing the dependence of the resultant model on the starting model. In order to avoid local minima, leading to erroneous velocity–depth models, we applied a further search using parameters that are significantly larger or smaller than those of the model. The resulting estimates of Moho depth are listed in Table 2.

In the second method, we adopted a Monte-Carlo scheme by randomly selecting velocity–depth models within a band of prescribed velocity–depth functions and comparing the synthetic with the observed receiver functions. This approach has the advantage that the depths to seismic discontinuities can be varied within the prescribed limits. A total of 20 000 random models were generated for each station. For each model, the variance was calculated as the squared difference between the observed and synthetic receiver function waveforms. The best model is defined as the one that gives minimum variance. We plot this model in Fig. 7 as the light solid lines for each station investigated. The models associated with variance estimates that have a maximal variance of up to 30 per cent are shown as dashed lines. The comparison of the observed and synthetic receiver functions calculated for the best model is presented in Fig. 8. The plots in Figs 7 and 8 represent the modelling of the sum of the move-out-corrected receiver functions compared with a single synthetic calculated for the reference slowness of 6.4 s deg^{-1}. We obtained multiple model estimates by forming sums of subsets of the data and repeating the Monte-Carlo analysis. Based on all the model estimates with variance of less than 30 per cent, approximately several hundreds for each station, we could derive estimates for the standard errors of crustal thickness and of subMoho upper-mantle velocities. The results are summarized in Table 3.

The seismograms shown in Figs 6 and 8 contain high frequencies (low-pass cut-off at 0.5 Hz), so multiples associated with the *P–S* conversion from the Moho are not clearly visible in these traces. However, in the low-pass filtered traces of Figs 5 and 9 the Moho multiples are more easily recognized. Thus, we repeated the receiver function modelling on the low-pass filtered stacked receiver functions in an attempt to better resolve structure in the upper mantle (Fig. 9). Fig. 9 not only illustrates prominent Moho multiples, but also provides evidence for an upper-mantle low-velocity zone (LVZ) beginning at depths of 60–70 km beneath some of the stations. The LVZ is characterized in the receiver functions by negative amplitude in the time range between 5 and 10 s and by associated multiples at times between 20 and 30 s. Receiver function synthetics are shown for the initial models with a simplified crustal structure and a homogeneous velocity in the upper mantle. The evidence for the presence of an upper-mantle LVZ is clearest for station BGIO. At this station, as well as others, the negative amplitude at 5–10 s delay time requires a LVZ in the upper mantle. There is no clear indication for an upper-mantle LVZ beneath HITJ, whereas at KEG the evidence is marginal. The phase seen between 25 and 30 s at KEG could well be a multiple associated with a *P–S* conversion from a LVZ located at greater depth, that is, at approximately 80 to 90 km.

7 THE CRUST AND UPPER-MANTLE LID

Below we describe the velocity–depth models obtained at each station (see Figs 6 and 7). First we describe stations that are located

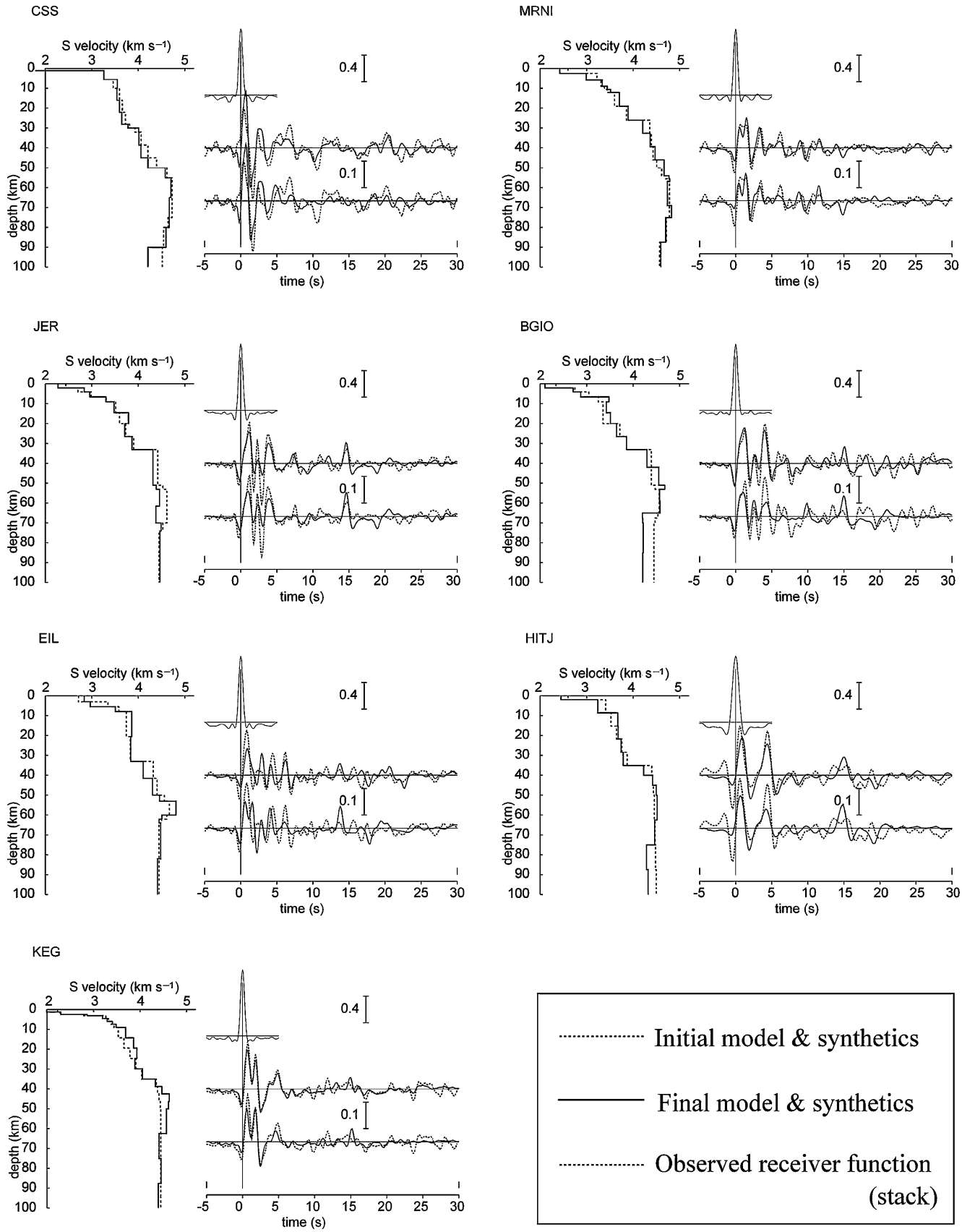

Figure 6. Results of the inversion for the stations investigated. For a given station the starting velocity–depth model (lighter line) and final model (thick line) are presented on the left, and waveforms on the right. The waveforms are further divided into: *P* waveform (L component) obtained after deconvolution and stacking in the upper part; observed and stacked waveforms (dashed lines) and synthetic waveforms (solid lines) of the Q component for the initial model (bottom trace) and final model (middle trace). Vertical bars next to the waveform traces indicate the normalized amplitudes.

Table 2. Observed delay times T (P_bs) of P–S waves converted at the top of basement, inferred basement depths and shear wave velocities in the surface layer (V_{s1}) and basement (V_{s2}). The values were obtained using the Monte-Carlo inversion method. Estimates of standard errors are also given. The Vp/Vs ratio was fixed at 1.78 in the top layer and 1.73 in the basement.

Station	T (P_bs) (s)	Depth to basement (km)	V_{s1} (km s^{-1})	V_{s2} (km s^{-1})
CSS	0.40	1.9 ± 0.5	2.32 ± 0.31	3.64 ± 0.06
MRNI	0.55	2.3 ± 0.3	2.48 ± 0.13	3.47 ± 0.05
JER	1.15	5.5 ± 1.0	2.76 ± 0.16	3.56 ± 0.09
BGIO	0.85	3.4 ± 0.9	2.54 ± 0.13	3.47 ± 0.08
EIL	0.85	3.2 ± 0.9	2.50 ± 0.14	3.54 ± 0.07
HITJ	0.40	1.7 ± 0.5	2.43 ± 0.11	3.60 ± 0.06
KEG	0.70	2.8 ± 0.3	2.41 ± 0.16	3.55 ± 0.09

in purely continental regions, that is, KEG and HITJ. Then we describe the structure beneath the stations located close to the DSF and the Cyprus arc representing major tectonic features of the Sinai subplate. The observations related to basement depth and the crust–mantle boundary and their interpretations are also given in Tables 2 and 3.

8 KEG

The station is located within the African Plate approximately 50 km west of the northern end of the Gulf of Suez, which delineates the western boundary of the Sinai subplate (Fig. 1). There is a strong conversion at the bottom of the sedimentary sequence at 0.7 s, followed by a multiple, and also a conversion from the Moho discontinuity at 4.8 s, again followed by a multiple between the free surface and the Moho. The model yields a value of 2.8 km for the depth to the top of basement and a Moho depth of 36 km with a mantle S-wave velocity of 4.4–4.5 km s^{-1}. The inferred Moho depth is slightly higher than the estimate of 33 km reported by Sandvol *et al.* (1998b). This is not, in our view, a significant discrepancy because our estimate and that of Sandvol *et al.* (1998b) lie within the respective standard error estimates. We noticed, however, that the Moho could also be modelled by a transition extending over a 10-km depth interval with its centre at 33.4 ± 0.5 km. As mentioned above we try to keep the velocity model as simple as possible, so we prefer the former.

Several refraction, gravimetric and teleseismic receiver function studies have been conducted in the regions surrounding the Sinai Peninsula and the Eastern Desert of Egypt to estimate the crust and upper-mantle structure. Meshref (1990) reported that the crust west of KEG is continental in nature with a relatively simple structure consisting of a sedimentary layer of 3 km with a velocity of 3.5 km s^{-1}, overlying the upper and lower crust with a thickness of 30 km, with a moderate velocity change from 6.0 to 6.35 km s^{-1}. For the Gulf of Suez (Fig. 1), the northernmost part of the Red Sea, south and west of the Sinai Peninsula, the crustal thickness is 35 km (Makris *et al.* 1988, 1991) and a crustal thickness of 33 km beneath KEG in the Eastern Desert of Egypt (Sandvol *et al.* 1998b). A slightly thicker crust of 35 km in the northwest part of the Sinai Peninsula was reported by Ginzburg *et al.* (1979a,b). Rybakov *et al.* (1997), using newly compiled gravimetric and magnetic data, reconfirmed the results of earlier studies regarding the continental nature of the crust in Egypt (Meshref 1990), the Sinai Peninsula and the southern part of Israel (Folkman & Bein 1978). The lack of positive magnetic anomalies in the Sinai Peninsula and the small to moderate variations of the Bouguer gravity anomalies point to the rather small to moderate variations of the crust, in agreement with the above mentioned refraction studies. Thus, a representative average crustal thickness of the Eastern Desert of Egypt is approximately 33 to 35 km. Our results, suggesting a crustal thickness between 33 and 36 km, are in a good agreement with those studies.

9 HITJ

This station is located approximately 70 km east of the DSF (Fig. 1). There is a strong conversion from the bottom of the sedimentary sequence of approximately 2 km at 0.4 s (Table 2) and also a strong conversion from the Moho discontinuity at 4.4 s, followed by clear Moho multiples (Figs 5 and 9) between the free surface and the Moho arriving at approximately 15 s. The Moho depth is 34 ± 2 km with an upper-mantle S-wave velocity of 4.3–4.4 km s^{-1}. The velocity model is simple and continental in nature (Rybakov *et al.* 1997). These results are in good agreement with reports of the refraction studies of El-Isa *et al.* (1987a,b) and gravimetric studies (Al-Zoubi & Ben-Avraham 2002). The velocity structure, below the Moho discontinuity at depths of 50 to 60 km, shows no clear evidence for substantial velocity changes in the upper mantle.

10 EIL

This station is located on the margin of the DSF (Fig. 1). We see a clear conversion from the bottom of the sediments at 0.8–0.9 s, followed by a moderate multiple between the free surface and the bottom of the sedimentary sequence, and a clear conversion from the Moho discontinuity at 4.4 s. The inferred basement depth is approximately 3 km (Table 2). The inferred Moho depth is between 33 and 35 km, depending on the inversion method used, with a mantle S-wave velocity of 4.4 km s^{-1}. The clear conversion, which appears at approximately 6 s, suggests the existence of a mantle lid between depths of 53 to 62 km with a velocity increase of the S waves to 4.7 km s^{-1}. This phase shows up only for events lying in the easterly backazimuth (Fig. 3) suggesting that the mantle lid is a regional feature. The modelling of this mantle lid using multiples from a discontinuity within the crust led to a complicated and unrealistic model, which was therefore discarded.

11 BGIO

This station is located approximately 40 km west of the DSF (Fig. 1). There is a strong conversion at the bottom of the sedimentary sequence at 0.–0.9 s, followed by a multiple, and also a second strong conversion from the Moho discontinuity at 4.1 s, again followed by a moderate multiple between the free surface and the Moho. The inferred depth to basement is 3.4 ± 0.9 km (Table 2). The Moho depth is 32–33 km with a mantle S-wave velocity of 4.4 km s^{-1}. A moderate conversion at approximately 6–7 s suggests the existence of a mantle lid between depths of 53 to 65 km with a velocity increase of the S waves to 4.6 km s^{-1}. As at EIL, the upper-mantle lid may be restricted to observations from the easterly backazimuth (Fig. 3).

12 JER

This station is located approximately 10 km east of BGIO (Fig. 1) and therefore we used the final model of BGIO as the initial model for the station. Because the background noise at JER is higher than that of BGIO we expect somewhat poorer resolution. The velocity–depth model of the crust is essentially the same, but shows several

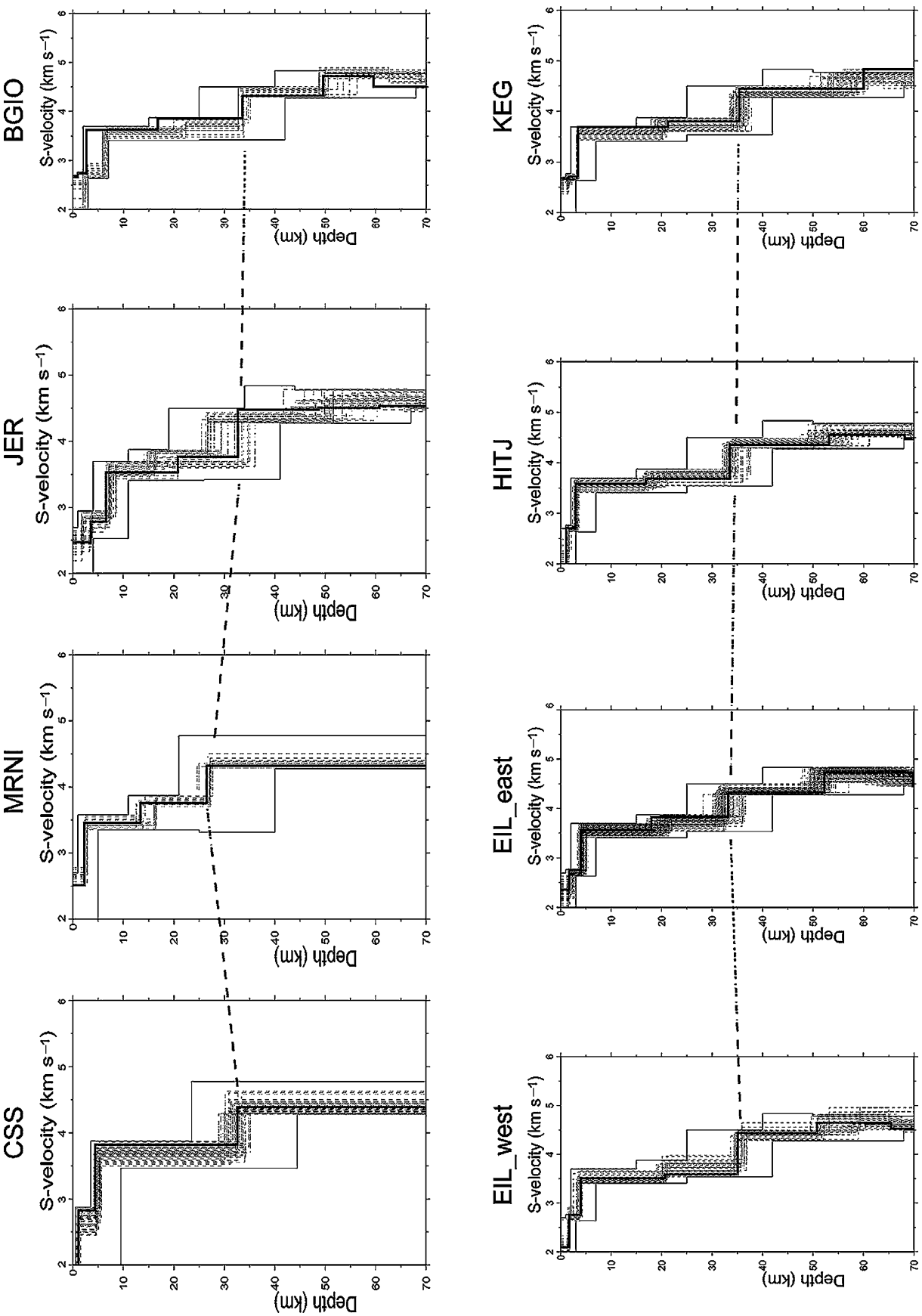

Figure 7. Crust and upper-mantle models obtained with Monte-Carlo modelling of the receiver functions as described in the text. The outer solid lines indicate the search bounds of the models. The thick solid line marks the best model giving the minimum variance estimate. Dashed lines mark models that are within 30 per cent of the variance estimate for the best model. Thick dashed lines between panels mark the inferred Moho depths.

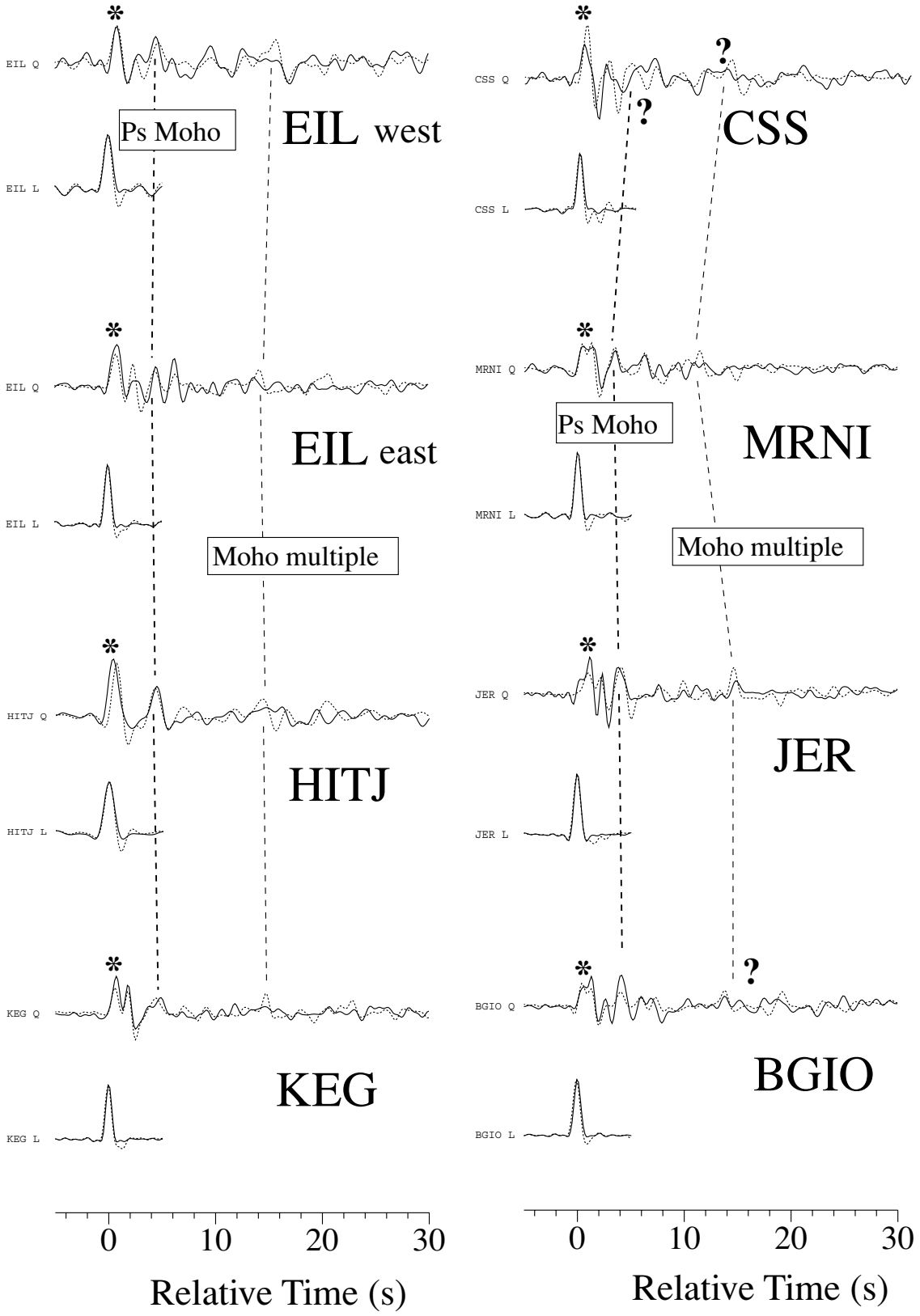

Figure 8. Comparison of observed stacked receiver functions (solid lines) with synthetic ones (dashed) calculated for the best models shown in Fig. 7. The short traces show the *P*-wave (L-component) seismograms. The solid line indicates the observed stacked *P*-wave seismogram. This is the one used as the input signal for the synthetic receiver function calculation. For comparison, we also show the theoretical L-component *P*-wave seismogram calculated for the best model. This shows a negative back swing and a *P*-wave peg-leg multiple between surface and bottom of the near-surface sedimentary layer, which is not seen in the observed seismogram. This is an artefact of the deconvolution where the inverse operator was determined for the *P*-wave group, which contained these multiples and, hence, the *P*-wave multiples do not show up in the observed trace.

Table 3. Observed delay times $T(P_Ms)$ of P–S waves converted at the Moho, inferred Moho depths and upper-mantle shear wave velocities based on two inversion methods. The first two entries without error estimates were obtained using the inversion method described by Kind *et al.* (1995); the two right hand columns give the values obtained using Monte-Carlo inversion including estimates of standard errors.

Station	T (P_Ms) (s)	Moho depth (km)	V_s (mantle) (km s^{-1})	Moho depth (km)	V_s (mantle) (km s^{-1})
CSS	5.5	32.0	4.33	31.8 ± 1.8	4.36 ± 0.03
MRNI	3.5	27.0	4.34	27.8 ± 0.8	4.42 ± 0.03
JER	4.0	32.0	4.44	31.5 ± 2.8	4.37 ± 0.09
BGIO	4.1	33.0	4.39	32.0 ± 2.0	4.46 ± 0.08
EIL	4.4	35.0	4.39	33.5 ± 1.8	4.34 ± 0.06
HITJ	4.4	34.0	4.28	34.1 ± 2.0	4.41 ± 0.08
KEG	4.8	36.0	4.39	35.6 ± 1.5	4.51 ± 0.11

minor differences. We see a clear conversion at the bottom of the sediments at 1.1 s, followed by a multiple between the free surface and the bottom of the sedimentary sequence, and a clear conversion from the Moho discontinuity at 4.0 s, again followed by a multiple between the free surface and the Moho. The basement depth is 5.5 ± 1.0 km (Table 2) and the Moho depth approximately 32 km, similar to BGIO, with an upper-mantle S-wave velocity of 4.4 km s^{-1}. The structure of a mantle lid at depths of 55 to 70 km is comparable to that at EIL and BGIO.

13 MRNI

This station is located 40 km west of the DSF (Fig. 1). There is a clear conversion at approximately 0.5–0.6 s followed by multiples. This conversion can be associated with a basement depth of approximately 2.3 km (Table 2). The P–S conversion from the Moho discontinuity arrives at 3.5 s delay time. The Moho depth is at 27–28 km with an upper-mantle S velocity of 4.3 km s^{-1}, slightly lower than values obtained from refraction studies. A moderate conversion at approximately 6 s delay time suggests the existence of a mantle lid between 54 and 75 km with a velocity increase of the S waves to 4.8 km s^{-1}.

14 CSS

This station is located roughly in the centre of Cyprus (Fig. 1) and on the eastern flank of the ophiolitic outcrop of the Troodos Massif (Gass & Masson-Smith 1963; Robertson 2000). The geological structure beneath the station is complex and represents both the ophiolitic sequence, with a thickness of 6 to 8 km, and the continental structure beneath, with a probable thickness of 20 to 25 km (Panayides, private communication; Makris & Wang 1995). There is a strong conversion at approximately 0.4 s delay time followed by a multiple. This conversion may originate at a shallow interface at approximately 2 km depth, which can be associated with the interface between the pillow lavas and the sheeted dykes. A low-amplitude conversion is seen at 2.3 s that we interpret as the conversion from the bottom of the oceanic crust. The deeper conversion at a depth of approximately 32 km is associated with the bottom of the continental crust or the Moho discontinuity. The strong phase that is seen at 7 s is a multiple from the bottom of the oceanic crust, which is probably superimposed on a P–S converted phase caused by a pronounced velocity increase between 50 and 80 km. This pronounced velocity increase probably reflects the complex structure in the proximity to the Cyprus arc and can be related to the subduction process there. It should be mentioned that in the analysis we obtained several different velocity models, which adequately match the observed receiver function, reflecting the inherent non-uniqueness of receiver function analysis (Ammon *et al.* 1990). Using independent information, such as geological data (Panayides, private communication), a refraction study (Makris & Wang 1995) and a gravimetric study (Ben-Avraham *et al.* 2002), we were able to discard the velocity models that did not match the independent information. As a result of the poor resolution, details of the deep structure are not clear.

15 COMPARISON OF RESULTS FROM EIL, HITJ, BGIO, JER AND MRNI WITH THOSE OF OTHER STUDIES

Fig. 10(a) shows the Moho depths beneath the broad-band stations in the vicinity of the DSF and their migrated seismograms along the north–south cross-section. These results are comparable to those presented in Fig. 1. The refraction studies of Ginzburg *et al.* (1979a,b, 1981), the study of Ginzburg & Folkman (1980) and the reflection study of Yuval & Rotstein (1987) report that the Moho discontinuity is located at approximately 32-km depth in the northernmost part of the Gulf of Aqaba and the crust gradually thins (the Moho shallows) towards the Mediterranean Sea. Thus, the modelled crustal thickness of 33–35 km for station EIL is in good agreement with the results of the above-mentioned studies. The crustal thickness of 34 km at HITJ, located on the margin of the Arabian Shield, agrees with earlier studies (El-Isa *et al.* 1987a,b; Rodgers *et al.* 1999). Sandvol *et al.* (1998), based on teleseismic receiver functions, reports a crustal thickness beneath station BGIO of 33 km, which agrees with our estimate. Based on gravimetric and magnetic data, Folkman & Bein (1978) suggested a change from continental type crust in southern Israel to a more mafic crust in the north. Later studies indicated similar conclusion, using gravimetric and magnetic data (Rybakov *et al.* 1997), reflection data (Frieslander *et al.* 1990), geological data (Hirsch & Picard 1988) and teleseismic traveltime residuals (Hofstetter *et al.* 1991, 2000). The change takes place along a mid-Jurassic E–W trend line and roughly coincides with the latitude of the northern part of the Dead Sea. Station BGIO is located near this border. Thus, the modelled crustal thickness of 33 km is in good agreement with the above-mentioned studies. North of BGIO, the Moho shallows and the crustal thickness of 27 km obtained below MRNI is in good agreement with the regional trend based on refraction studies (Ginzburg *et al.* 1979a,b; Ginzburg & Folkman 1980), Bouguer gravity anomalies (Kamal *et al.* 1993) and velocity anomalies from teleseismic tomography (Hofstetter *et al.* 2000).

16 UPPER-MANTLE STRUCTURE

Beneath several stations (BGIO, EIL, HITJ and MRNI) a first-order seismic discontinuity or a mantle lid appears at approximately 6 to 7 s, that is, at depths of approximately 53 to 65 km (see Figs 6 and 9). Ginzburg *et al.* (1979b, 1981) have reported an apparent mantle-P reflected phase of 8.6 km s^{-1} at a depth of 55 km along their profile from the southernmost part of the Gulf of Aqaba to the Dead Sea basin (for geographical location see Fig. 1). Profiles outside the DSF do not show this deep upper-mantle discontinuity. El (1990), using data from one station UNJ (located at approximately 32° N, 36° E; see Fig. 1) has noted such upper-mantle discontinuities starting at 55 km with a thickness of approximately 2 to 3 km and an apparent velocity of 8.4 km s^{-1} and a deeper one at a depth of 105 km with

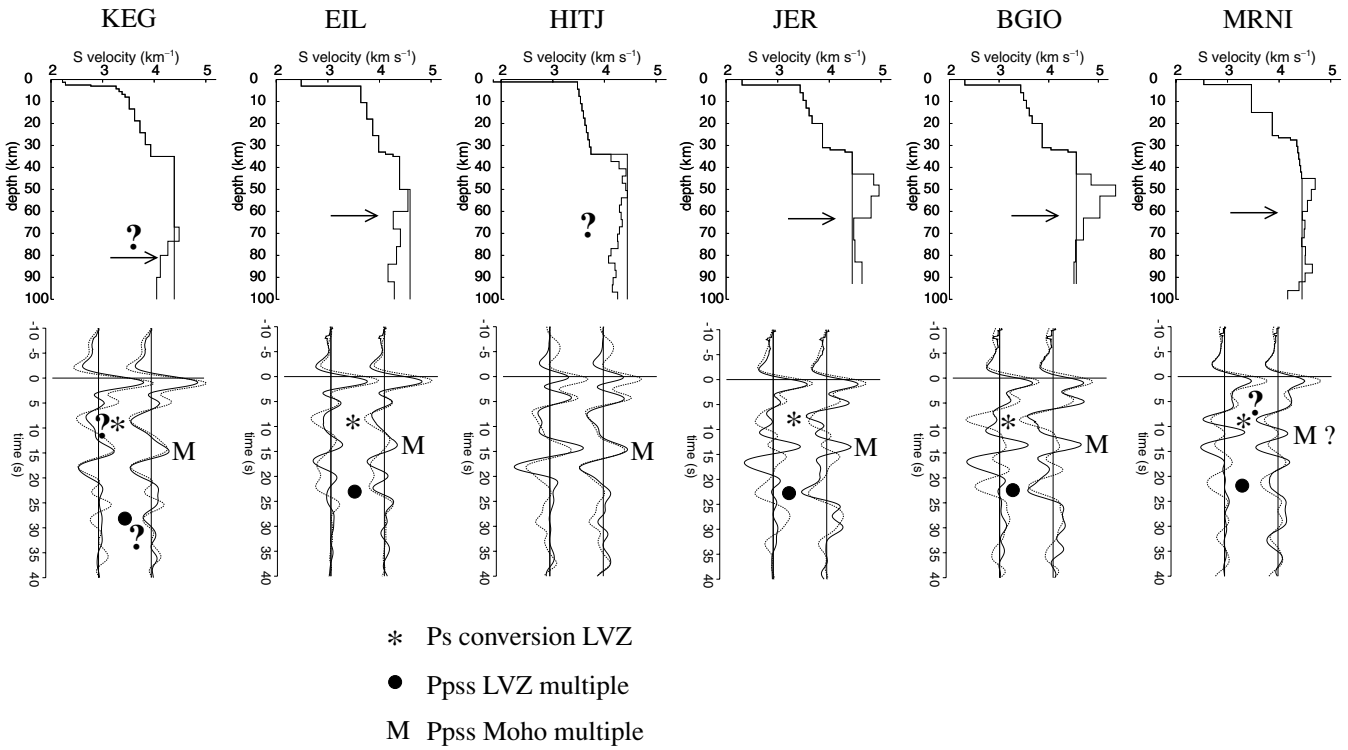

Figure 9. Phase interpretation for low-pass filtered receiver functions. The initial models contained the crustal structure estimated in an earlier step and a homogeneous mantle. Comparison of the observed and synthetic receiver function seismograms between the initial and final model suggests that an upper-mantle low-velocity zone (LVZ) is supported by the data where this is indicated by an arrow without a question mark. The asterisk indicates the negative amplitudes associated with *P–S* conversions from this LVZ, while the dots indicate the associated *Ppps* (negative amplitude and arriving first) and *Ppss* type (positive amplitude, arriving later) multiples seen between approximately 20 and 30 s. The first positive Moho *Ppps* multiple is indicated by the letter M.

an apparent velocity of 8.69 km s^{-1}. In between the refractors he inferred the presence of a LVZ reaching its minimum velocity at a depth of 80 km.

Our observations at the above-mentioned broad-band stations are in good agreement with a mantle refractor at a depth of 55 km. A velocity decrease beginning at approximately 60–70 km beneath EIL, JER, BGIO and perhaps also MRNI underlies the high-velocity mantle lid. This boundary possibly marks the seismic lithosphere–asthenosphere boundary (LAB). Positive identification of the LAB is made possible by the presence of associated multiples (Fig. 9). There is weak evidence that the depth of the LVZ is greater beneath KEG and HITJ. The very shallow depth for the LAB in the area of the DSF appears to indicate an upwelling asthenosphere, which may have influenced the evolution of the transform boundary between the Arabian and African plates along the DSF.

The LAB (Watts 2001) is normally defined using either seismological observations, where one searches for pronounced velocity change, that is, receiver function analysis or teleseismic tomography, or based on a thermal boundary layer that is normally correlated with the 1350 °C isotherm (Davis & Lister 1974; Parsons & McKenzie 1978). Using heat flow observations, Jimenez-Munt *et al.* (2003) suggested a lithopsheric thickness of 80 km in the east Mediterranean Sea. Based on petrological studies of mantle xenoliths in volcanic rocks in various parts of the Arabian massive, the LAB was defined to be between 60 to 75 km (Henjes-Kunst 1989; McGuire & Bohannon 1989; Altherr *et al.* 1990; Weinstein 1998). Furthermore, at a similar depth range velocity anomalies obtained from teleseismic tomography along large parts of the DSF and its flanks suggest a velocity decrease (Hofstetter *et al.* 2000). Our observations of velocity decrease beginning at approximately 60–70 km are in very good agreement with the above-mentioned observations.

Recent observations of shear wave splitting over the DSF between the Dead Sea basin and the Red Sea show substantial anisotropy parallel to the DSF, suggesting that there may be strong deformation in the mantle located directly beneath the DSF (Rümpker *et al.* 2000; Bock *et al.* 2001). The splitting observations can be explained by preferred alignment of olivine along the transform induced either by the shear movement of the opposing plates or by channelled subhorizontal flow in an upwelling asthenosphere beneath the transform, or a combination of the two processes. Our observations of a relatively shallow LAB under the DSF provide a constraint on the location of subhorizontal flow in the asthenosphere beneath the DSF.

17 THE TRANSITION ZONE

Finally, we briefly discuss the receiver function determinations in relation to the transition zone between the upper and lower mantles. This zone is bounded by the seismic discontinuities that occur globally at average depths of 410 and 660 km. Both discontinuities probably reflect phase transitions in the olivine mineral of mantle rock. The 410-km discontinuity is associated with the transition from olivine to wadsleyite (spinel β phase). The 660-km discontinuity is generally believed to represent the transition from ringwoodite (spinel γ phase) to a perovskite and magnesiowustite structure. The two transitions have a Clapeyron slope of opposite signs such that in cold mantle regions the 410-km discontinuity is elevated and the 660-km discontinuity is depressed yielding a wider depth range for

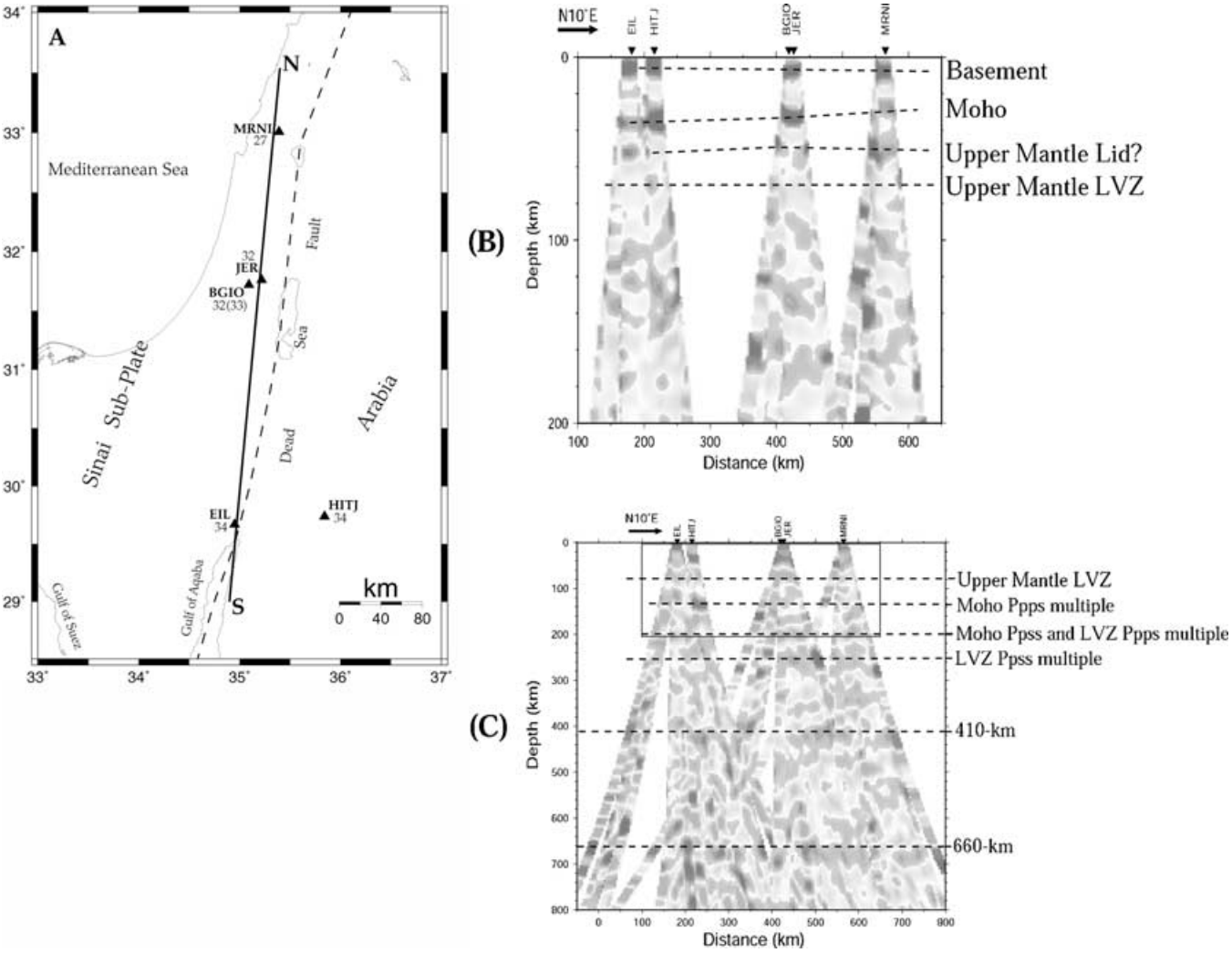

Figure 10. (a) Crustal thickness (km) at a given broad-band station along the cross-section N–S (solid line). Crustal thickness obtained by Sandvol *et al.* (1998b) for BGIO is given in parenthesis. The schematic DSF (dashed line) is shown as a reference. (b) Migrated depth sections projected along the N–S line in (a). The time-dependent seismograms were migrated to depth along the backazimuthal direction of the *P–S* converted wave assuming the IASPEI91 reference model (Kennett & Engdahl 1991). Dark gery indicates positive amplitudes (i.e. velocity increases with increasing depth if this is associated with a *P–S* conversion), while light gery indicates negative amplitudes (i.e. velocity decreases with depth). Various *P–S* converted phases are labelled indicating their origin. The panel was derived from high-frequency receiver functions (low-pass filtered with 0.5 Hz corner frequency). (c) The panel is based on long-period receiver functions (low-pass filtered with 0.2 Hz corner frequency). This enhances *P–S* conversions from the mantle discontinuities at 410 and 660 km (see also Fig. 5), but the *P–S* conversion from the Moho is less well resolved than in (b). Multiples from the Moho and the upper-mantle low-velocity zone (LVZ) are indicated. *Ppps* is a multiple with a *P*-wave reflection from the surface and a *P–S* reflection from the seismic discontinuity at depth. They have the same polarity as the primary *P–S* phases converted at the same discontinuity. The *Ppss* is a multiple consisting of a *P–S* reflection from the surface and an *S–S* reflection from the seismic discontinuity. Its polarity is opposite to that of the associated primary conversion.

the transition zone. In hot mantle regions, the opposite effect is observed with the 410-discontinuity being depressed and the 660-km discontinuity being elevated resulting in a narrower transition zone (Gossler & Kind 1996).

The *P–S* conversions from the 410- and 660-km discontinuities can be recognized in Fig. 5. They are observed most clearly at stations MRNI, JER and BGIO. The 410-km discontinuity is also seen at stations CSS and EIL, but there is no clear phase that can be easily associated with a *P–S* conversion from the 660-km discontinuity. At HITJ and KEG, possible *P–S* conversions from the mantle discontinuities have been marked, but they do not clearly stand out against neighbouring phases. Measuring the peak amplitudes of the *P–S* conversions, a value of 24.4 $\pm$ 0.9 s is obtained for the differential time $P\,660 - P\,410$ s. This time is close to that expected for the IASPEI91 model (Kennett & Engdahl 1991), that is, 23.9 s. This suggests that mantle temperature in the transition zone is close to normal. However, absolute times of *P–S* conversions from both the 410- and 660-km discontinuities are late by approximately 2 s relative to the IASPEI91 model. This would suggest that the crust and mantle above 410-km depth have *S*-wave velocities that are, on average, approximately 2 per cent lower than those of the IASPEI model.

18 CONCLUSIONS

The results presented above and those of earlier studies suggest that the Sinai subplate is a transition zone between the thick continental crust of the Arabian shield and the relatively thin oceanic crust of the

eastern Mediterranean Sea. Refraction, reflection and gravimetric studies have shown that the Moho in the Sinai subplate generally shallows towards the northwest. Our results derived from teleseismic receiver functions, confirm this large-scale trend. At the Cyprus arc a crustal thickness of approximately 28 km is indicated, which is consistent with the complex ophiolitic sequence known to be present. Crustal thickness along the eastern part of the Sinai subplate, near the DSF, seems to increase from approximately 27 km northwest of the Sea of Galilee to approximately 32–33 km near the Dead Sea and north of the Gulf of Aqaba. No significant increase in crustal thickness is observed east of the DSF, between the Dead Sea and the Gulf of Aqaba towards the Arabian shield region, as evidenced by data from one station located in Jordan. A 35–36-km thick crust is inferred at station KEG located west of the Sinai subplate on the African plate.

At stations located close to the DSF, a mantle LVZ is observed, which is interpreted as the LAB. The LAB is located at shallow depth, beginning at approximately 60 km. The LAB is overlain by a mantle lid possessing high velocities and marking a refracting horizon, which has previously been inferred from refraction seismic data. These observations are in good agreement with petrological studies of volcanic rocks in various parts of the Arabian massive, heat flow observations and velocity anomalies along the DSF and its flanks obtained from teleseismic tomography. It seems that near the DSF the lithosphere is thinned and this may mark a zone of weakness in the upper mantle where strong deformation was facilitated, eventually leading to the development of the DSF forming a large shear zone extending through the whole lithosphere.

The seismic mantle discontinuities at 410- and 660-km depth are observed clearly at stations near the DSF. Their vertical separation is close to the value expected from reference models of the Earth such as IASPEI91, suggesting that mantle temperatures are close to normal in the transition zone between upper and lower mantle. The *P–S* converted phases from the discontinuities, however, are delayed by approximately 2 s relative to IASPEI91, which requires lower-than-normal seismic velocities in the crust and mantle above 410-km depth. Under the Cyprus arc station and beneath the station KEG located on the African Plate, the mantle discontinuities, particularly at 660-km depth, are less clearly observed and their associated *P–S* converted phases may be closer to the theoretical times predicted by the IASPEI91 reference model.

A refinement of our results is expected for the area located between the Dead Sea and Red Sea where the large-scale passive seismic Dead Sea Rift Transect (DESERT) experiment, a joint effort by institutions in Germany, Jordan, Palestinian Authority and Israel, was recently concluded (Abu-Ayyash *et al.* 2000; Mohsen *et al.* 2001).

ACKNOWLEDGMENTS

The authors thank W. Hanka, GFZ, B. Reich, GII, and K. Solomi, GSC, for technical support in acquiring and processing the data. The authors also thank S. Mazza and A. Morelli, MedNet, for their support in obtaining KEG data, and S. Ruppert and J. O'Boyle, LLNL, for their support in obtaining HITJ data. The authors are grateful for the help of X. Li and X. Yuan of GFZ Potsdam in processing the data. The authors thank R. Kind for critical and constructive discussion and comments. Discussion and constructive comments on the geology of Cyprus with S. Kramvis, I. Panayides, K. Solomi and S. Eleftheriou, Geol. Survey of Cyprus, and J. Makris, Hamburg Univ., helped to improve the manuscript. The GeoForschungsZentrum, Potsdam, Germany, and the Earth Science Research Administration, the Ministry of the National Infrastructure, Israel, supported this study. Several figures in this report were prepared using the GMT programme (Wessel & Smith 1991).

REFERENCES

Abu-Ayyash, K. et al, 2000. Multinational geoscientific research effort kicks off in the Middle East, *EOS, Trans. Am. geophys. Un.,* **81(50),** 609–617.

Altherr, R., Henjes-Kunst, F. & Baumann, A., 1990. Asthenosphere versus lithosphere as possible sources for basaltic magmas erupted during formation of the Red Sea: Constraints from Sr, Pb and Nd isotopes, *Earth planet. Sci. Lett.,* **96,** 269–286.

Al-Zoubi, A. & Ben-Avraham, Z., 2002. Structure of the earth's crust in Jordan from potential field data, *Tectonophysics,* **346,** 45–59.

Ammon, C., Randall, G. & Zandt, G., 1990. On the nonuniqueness of receiver function inversion, *J. geophys. Res.,* **95,** 15 303–15 318.

Baker, J., Snee, L. & Menzies, M., 1996. A brief Oligocene period of flood volcanism in Yemen: Implication for the duration and rate of continental flood volcanism at the Afro-Arabian triple junction, *Earth planet. Sci. Lett.,* **138,** 39–55.

Ben-Avraham, Z. & Ginzburg, A., 1990. Displaced terranes and crustal evolution of the Levant and the eastern Mediterranean, *Tectonics,* **9,** 613–622.

Ben Avraham, Z., Hanel, R. & Villinger, H., 1978. Heat flow through the Dead Sea rift, *Mar. Geol.,* **28,** 253–269.

Ben-Avraham, Z., Ginzburg, A., Makris, J. & Eppelbaum, L., 2002. Crustal structure of the Levant basin, eastern Mediterranean, *Tectonophysics,* **346,** 23–43.

Bock, G., Hofstetter, A., Mohsen, A., Rümpker, G. & DESERT Group, 2001. Evidence for olivine alignment parallel to the Dead Sea Transform from shear wave splitting analysis. In: *AGU Fall Meeting, December 2001*.

Burdick, L. & Langston, C., 1977. Modeling crustal structure through the use of converted phases in teleseismic body waveforms, *Bull. seism. Soc. Am.,* **67,** 677–691.

Camp, V.E. & Roobol, M.J., 1992. Upwelling asthenosphere beneath western Arabia and its regional implications, *J. geophys. Res.,* **97,** 15 255–15 271.

Christensen, N, 1996. Poisson's ratio and crustal seismology, *J. geophys. Res.,* **101,** 3139–3156.

Courtillot, V., Jaupart, C., Manighetti, I., Tapponnier, P. & Besse, J., 1999. On the causal links between flood basalts and continental breakup, *Earth planet. Sci. Lett.,* **166,** 177–195.

Davis, E. & Lister, C., 1974. Fundamentals of ridge crest topography, *Earth planet. Sci. Lett.,* **21,** 405–413.

Debayle, E., Lévêque, J.-J. & Cara, M., 2001. Seismic evidence for a deeply rooted low-velocity anomaly in the upper mantle beneath the northeastern Afro/Arabian continent, *Earth planet. Sci. Lett.,* **193,** 423–436.

El-Isa, Z., 1990. Lithospheric structure of the Jordan-dead Sea transform from earthquake data, *Tectonophysics,* **180,** 29–36.

El-Isa, Z., Mechie J., Prodehl, C., Makris, J. & Rihm, R., 1987a. A crustal structure study of Jordan derived from seismic refraction data, *Tectonophysics,* **138,** 235–253.

El-Isa, Z., Mechie J. & Prodehl, C., 1987b. Shear velocity structure of Jordan from explosion seismic data, *Geophys. J. R. astr. Soc.,* **138,** 265–281.

Feigin, G. & Shapira, A., 1994. *A unified crustal model for calculating travel times of seismic waves across the Israel Seismic Network, IPRG Rep. Z1/567/79(107)*.

Folkman, Y. & Bein, A., 1978. Geophysical evidence for a pre-late Jurassic fossil continental margin oriented east-west under central Israel, *Earth planet. Sci. Lett.,* **39,** 335–340.

Frieslander, U., Rotstein, Y., Derin, B. & Trachtman, P., 1990. Paleozoic basins in central Israel. In: *Isr. Geol. Soc. Annual Meet., Eilat*.

Garfunkel, Z., 1981. Internal structure of the Dead Sea leaky transform (rift) in relation to plate kinematics, *Tectonophysics*, **80,** 81–108.

Garfunkel, Z. & Horowitz, A., 1966. The upper Tertiary and the Quaternary morphology of the Negev, *Isr. J. Earth Sci.,* **15,** 101–117.

Gass, I. & Masson-Smith, D., 1963. The geology and gravity anomalies of the Troodos Massif, Cyprus, *Phil. Trans. R. Soc. Lond.,* A. **255,** 417–467.

Ginzburg, A. & Folkman, Y., 1980. The crustal structure between the Dead Sea rift and the Mediterranean Sea, *Earth planet. Sci. Lett.,* **51,** 181–188.

Ginzburg, A., Makris, J., Fuchs, K., Prodehl, C., Kaminski, W. & Amitai, U., 1979a. A seismic study of the crust and upper mantle of the Jordan-Dead Sea rift and their transition toward the Mediterranean Sea, *J. geophys. Res.,* **84,** 1569–1582.

Ginzburg, A., Makris, J., Fuchs, K., Perathoner, B. & Prodehl, C., 1979b. Detailed structure of the crust and upper mantle along the Jordan-Dead Sea rift, *J. geophys. Res.,* **84,** 5605–5612.

Ginzburg, A., Makris, J., Fuchs, K. & Prodehl, C., 1981. The structure of the crust and upper mantle in the Dead Sea rift, *Tectonophysics,* **80,** 109–119.

Ginzburg, A., Ben-Avraham, Z., Makris, J., Hubral, P. & Rotstein, Y., 1994. Crustal structure of northern Israel, *Mar. & Petroleum Geol.,* **11,** 501–506.

Gök, R., Turkelli, N., Sandvol, E., Seber, D. & Barazangi, M., 2000. Regional wave propagation in Turkey and surrounding regions, *Geophys. Res. Lett.,* **27,** 429–432.

Gossler, J. & Kind, R., 1996. Seismic evidence for very deep roots of continents, *Earth planet. Sci. Lett.,* **138,** 1–13.

Hearn, T. & Ni, J., 1994. *Pn* velocities beneath continental collision zones: the Turkish-Iranian plateau, *Geophys. J. Int.,* **117,** 273–283.

Heimann, A., Steinitz, G., Mor, D. & Shaliv, G., 1996. The Cover Basalt Formation, its age, and its regional and tectonic setting: Implication from K-Ar and ^{40}Ar/^{39}Ar geochronology, *Isr. J. Earth Sci.,* **45,** 55–71.

Henjes-Kunst, F., 1989. Mantle xenoliths in western Arabia and their bearing on asthenosphere–lithosphere dynamics during formation of the Red Sea Rift—A review. In: *Spannung und Spannungsumwandlung in der lithosphare, Symposium on the Afro-Arabian Rift System*, pp. 49–50, Karlsruhe University, Karlsruhe, Germany.

Hirsch, F. & Picard, L., 1988. The Jurassic facies in the Levant, *J. Petroleum Geol.,* **11,** 277–308.

Hofmann, C., Courtillot, V., Féraud, G., Rochette, P., Yirgu, G., Ketefo, E. & Pik, R., 1997. Timing of the Ethiopian flood basalts event and implications for plume birth and global change, *Nature,* **389,** 838–841.

Hofstetter, A., 1996. *Determination of body-wave and surface-wave magnitude of regional and teleseismic earthquakes using the broad band station at Bar Giora, IPRG Rep., 567/30/96*.

Hofstetter, A., Feldman, L. & Rotstein, Y., 1991. Crustal structure of Israel: constraints from teleseismic and gravity data, *Geophys. J. Int.,* **104,** 371–379.

Hofstetter, A., Dorbath, C., Rybakov, M. & Goldshmidt, V., 2000. Crustal and upper mantle structure across the Dead Sea rift and Israel from teleseismic P wave tomography and gravity data, *Tectonophysics,* **327,** 37–59.

Jimenez-Munt, I., Sabadini, R., Gardi, A. & Bianco, G., 2003. Active deformation in the Mediterranean from Gibralter to Anatolia inferred from numerical modeling and geodetic and seismological data, *J. geophys. Res.,* **108,** 2006–2024.

Kamal, K., Khawlie, M., Haddad, F., Barazangi, M., Seber, D. & Chaimov, T., 1993. Bouguer gravity and crustal structure of the Dead Sea transform fault and adjacent mountain belts in Lebanon, *Geology,* **21,** 739–742.

Kennett, B.L.N. & Engdahl, E.R., 1991. Traveltimes for global earthquake location and phase idenfication, *Geophys. J. Int.,* **105,** 429–465.

Kind, R., Kosarev, G. & Petersen, N., 1995. Receiver functions at the stations of the German Regional Seismic Network (GRSN), *Geophys. J. Int.,* **121,** 191–202.

Knox, R., Nyblade, A. & Langston, C., 1998. Upper mantle S velocities beneath Afar and western Saudi Arabia from Rayleigh wave dispersion, *Geophys. Res. Lett.,* **25,** 4233–4236.

Kumar, M.R., Ramesh, D.S., Saul, J., Sarkar, D. & Kind, R., 2002. Crustal structure and upper mantle stratigraphy of the Arabian shield, *Geophys. Res. Lett.,* **29,** in press.

Langston, C., 1977. The effect of planar dipping structure on source and receiver responses for constant ray parameter, *Bull. seism. Soc. Am.,* **67,** 1029–1050.

Langston, C., 1979. Structure under Mount Rainier, Washington, inferred from teleseismic body waves, *J. geophys. Res.,* **84,** 4749–4762.

Makris, J. & Wang, J., 1995. *Geophysical study and geodynamics of the Eastern Mediterranean Sea, Rep. 719/48–1* Inst. Geophys., Univ. of Hamburg, Hamburg.

Makris, J., Ben-Avraham, Z., Behle, A. Ginzburg, A., Giese, P., Steinmetz, L., Whitmarsh, R. & Eleftheriou, S., 1983. Seismic refraction profiles between Cyprus and Israel and their interpretation, *Geophys. J. R. astr. Soc.,* **75,** 575–591.

Makris, J., Rihm, R. & Allam, A., 1988. Some geophysical aspects of the evolution and the structure of the crust in Egypt, in, *The Pan-African Belt of Northeast Africa and the Adjacent Area*, pp. 345–369, eds Gaby, S.El & Greiling, R.O.

Makris, J., Henke, C., Egloff, F. & Akamaluk, T., 1991. The gravity field of the Red Sea and East Africa, *Tectonophysics,* **198,** 369–381.

Makris, J., Wang, S., Odintsov, S. & Udintsev, G., 1994. The magnetic field of the eastern Mediterranean Sea, in, Geological Structure of the Northern Mediterranean, pp. 75–87, eds Krasheninnikov, V. & Hall, J., Jerusalem.

Matmon, A., Zilberman, E. & Enzel, Y., 2000. Determination of escarpment age using morphologic analysis: an example from the Galilee, northern Israel, *Geol. soc. Am. Bull.,* **112,** 1864–1876.

McGuire, A.V. & Bohannon, R.G., 1989. Timing of mantle upwelling: evidence for a passive origin for the Red Sea rift, *J. geophys. Res.,* **94,** 1677–1682.

Mellors, R., Vernon, F., Camp, V., Al-Amri, A., Ghalib, A. & Al-Dail, M., 1999. Regional waveform propagation in the Saudi Arabian peninsula, *Geophys. Res. Lett.*, in press.

Meshref, W., 1990. Tectonic framework, in, *The Geology of Egypt*, pp. 113–156, ed. Rushdi Said

Mohsen, A., Bock, G., Abdel-Hafez, W., Hofstetter, A., Rümpker, G., El-Kelani, R., Wylegalla, K. & DESERT2000 Working Group, 2001. A passive seismic array across the Dead Sea transform. In: *EGS Meeting, March 2001*.

Owens, T., Zandt, G. & Taylor, S., 1984. Seismic evidence for an ancient rift beneath the Cumberland Plateau, Tennessee: A detailed study analysis of broadband teleseismic P waveforms, *J. geophys. Res.,* **89,** 7783–7795.

Parsons, B. & McKenzie, D., 1978. Mantle convection and the thermal structure of plates, *J. geophys. Res.,* **83,** 4485–4496.

Picard, L., 1951. Geomorphogeny of Israel, *Negev. Res. Counc. Bull.,* **8,** 1–30.

Robertson, R., 2000. Tectonic evolution of Cyprus in its Easternmost Mediterranean setting. In: *Proceed. Third Intern. Conf. on the Geology of the Eastern Mediterranean*, pp. 11–44, eds Panayides, I., Xenophontos, C. & Malpas, J.

Rodgers, A., Ni, J. & Hearn, T., 1997. Propagation characteristics of short-period *Sn* and Lg in the Middle East, *Bull. seism. Soc. Am.,* **87,** 396–413.

Rodgers, A., Walter, W., Mellors, R, Al-Amri, A. & Zhang, Y., 1999. Lithospheric structure of the Arabian shield and platform from complete regional waveform modeling and surface wave group velocities, *Geophys. J. Int.,* **138,** 871–878.

Rümpker, G., Ryberg, T. & Bock, G., 2000. High-resolution SKS splitting measurements across the Dead Sea Transform. In: *AGU Fall Meeting 2000*.

Rybakov, M., Goldshmidt, V. & Rotstein, Y., 1997. New compilation of the gravity and magnetic maps of the Levant, *Geophys. Res. Lett.,* **24,** 33–36.

Salamon, A., Hofstetter, A., Garfunkel, Z. & Ron, H., 1996. Seismicity of Eastern Mediterranean Region: Perspective from the Sinai subplate, *Tectonophysics,* **263,** 293–305.

Sandvol, E., Seber, D., Barazangi, M., Vernon, F., Mellors, R. & Al-Amri, A., 1998a. Lithospheric seismic velocity beneath the Arabian Shield, *Geophys. Res. Lett.,* **25,** 2873–2876.

Sandvol, E., Seber, D., Calvert, A. & Barazangi, M., 1998b. Grid search modeling of receiver functions: Implications for crustal structure in the Middle East and North Africa, *J. geophys. Res.,* **103,** 26 899–26 917.

Sandvol, E. *et al.*, 2001. Tomographic imaging of Lg and *Sn* propagation in the Middle East, *Pure appl. Geophys.,* **158,** 1121–1163.

Segev, A., 2000. Synchronous magmatic cycles during the fragmentation of Gondwana: radiometric ages from the Levant and other provinces, *Tectonophysics,* **325,** 257–277.

Shamir, G., 1995. The broadband station at Bar Giora. In:, *Annual Meeting Isr. Geol. Soc., 98*.

Sneh, A., 1996. The Dead Sea Rift: lateral displacement and downfaulting phases, *Tectonophysics,* **263,** 277–292.

Stammler, K., 1993. SeismicHandler—programmable multichannel data handler for interactive and automatic processing of seismological analyses, *Computers and Geosciences,* **19,** 135–140.

Vinnik, L.P., 1977. Detections of waves converted from P to SV in the mantle, *Phys. Earth planet. Int.,* **15,** 39–45.

Watts, A., 2001. *Isostasy and flexure of the Lithosphere*, Cambridge Univ. Press, Cambridge, p. 458.

Weinstein, Y.S., 1998. Mechanisms of generation of intra-continental alkali-basalts in northeastern Israel, *PhD thesis* The Hebrew Univ., Jerusalem, p. 101.

Wessel, P. & Smith, W., 1991. Free software helps maps and display data, *EOS, Trans. Am. geophys. Un.,* **72,** 441.

Yuan, X., Ni, J., Kind, R., Mechie, J. & Sandvol, E., 1997. Lithospheric and upper-mantle structure of southern Tibet from a seismological passive source experiment, *J. geophys. Res.,* **102,** 27 491–27 500.

Yuval, Z. & Rotstein, Y., 1987. Deep crustal reflection survey in central Israel, *J. Geodyn.,* **8,** 17–31.